Partonic Transverse Motion in Unpolarized Semi-Inclusive Deep Inelastic Scattering Processes

M. Boglione,[1] S. Melis,[2] and A. Prokudin[3]

[1] *Dipartimento di Fisica Teorica, Università di Torino, Via P. Giuria 1, I-10125 Torino, Italy*
INFN, Sezione di Torino, Via P. Giuria 1, I-10125 Torino, Italy
[2] *European Centre for Theoretical Studies in Nuclear Physics and Related Areas (ECT*)*
Villa Tambosi, Strada delle Tabarelle 286, I-38123 Villazzano, Trento, Italy
[3] *Jefferson Laboratory, 12000 Jefferson Avenue, Newport News, VA 23606*

We analyse the role of partonic transverse motion in unpolarized Semi-Inclusive Deep Inelastic Scattering (SIDIS) processes. Imposing appropriate kinematical conditions, we find some constraints which fix an upper limit to the range of allowed $k_\perp$ values. We show that, applying these additional requirements on the partonic kinematics, we obtain different results with respect to the usual phenomenological approach based on the Gaussian smearing with analytical integration over an unlimited range of $k_\perp$ values. These variations are particularly interesting for some observables, like the $\langle \cos\phi_h \rangle$ azimuthal modulation of the unpolarized SIDIS cross section or the average transverse momentum of the final, detected hadron.

PACS numbers: 13.88.+e, 13.60.-r, 13.85.Ni

INTRODUCTION

Inclusive and Semi-Inclusive Deep Inelastic Scattering (DIS and SIDIS) processes are important tools to understand the structure of nucleons and nuclei. Spin asymmetries in polarized SIDIS are directly related to Transverse Momentum Dependent (TMD) parton distribution and fragmentation functions, and are the subject of intense theoretical and experimental studies. The usual, collinear parton distribution functions depend on the fraction x_B of hadron momentum carried by the scattering parton and on the virtuality of the probe, Q^2. TMDs additionally depend on the intrinsic transverse momentum of the parton, $\boldsymbol{k}_\perp$, opening invaluable opportunities to unravel the three-dimensional partonic picture of the nucleon in momentum space.

At leading twist, the spin structure of a spin-1/2 hadron can be described by eight TMDs [1–3]. TMDs represents particular physical aspects of spin-orbit correlations at the partonic level. The dependence of the SIDIS cross section on the azimuthal angle, ϕ_h, of the electro-produced hadron with respect to the lepton scattering plane and on the nucleon polarization azimuthal angle, ϕ_S, allows a term by term separation of the different azimuthal contributions to the measured unpolarized and polarized cross sections and spin asymmetries.

The unpolarized SIDIS cross-section can be used not only to study the unpolarized TMD distribution function $f_{q/p}(x, k_\perp)$ and the unpolarized TMD fragmentation function $D_{h/q}(z, p_\perp)$, that encode the intrinsic dynamics of unpolarized partons, but also the Boer-Mulders distribution and the Collins fragmentation functions, which carry information about the dynamics of transversely polarized partons inside hadrons and give rise, for instance, to a $\cos 2\phi_h$ modulation of the unpolarized cross section. The existence of partonic intrinsic transverse momenta is also unequivocally signaled, in the unpolarized SIDIS cross section, by a $\cos\phi_h$ modulation, which is a subleading twist effect, suppressed by one power of Q. This contribution to the unpolarized cross section consists of a purely kinematical term, the Cahn effect [4, 5], proportional to the convolution of unpolarized distribution and fragmentation functions, and a term proportional to the convolution of the Boer-Mulders and the Collins functions, together with other twist-3 contributions, as pointed out in Ref. [2].

Polarized SIDIS experiments, in addition, allow us to explore the other TMDs which describe the dynamics of polarized and unpolarized partons inside polarized nucleons, such as the helicity, transversity and Sivers functions. These will not be considered in this paper.

TMD factorization theorems [6] are proven for SIDIS at momentum scales $Q \gg P_T \sim \Lambda_{QCD}$; here large Q values are needed to allow a perturbative treatment of the underlying partonic subprocess, while the small scale P_T ensures that the observables are sensitive to the intrinsic parton motion. Moreover, the smallness of intrinsic quark momenta is also explicitly required, as this approach is based on a series expansion in terms of the ratio $k_\perp/Q$ and higher orders are usually neglected. However, the present knowledge of TMDs and azimuthal asymmetries is mainly based on the available experimental data from the HERMES and COMPASS Collaborations, that operate at relatively low Q^2 values: typically, the cut $Q^2 > 1$ GeV^2 is assumed in order to ensure SIDIS kinematics.

Very often, in phenomenological analysis, the transverse momentum distribution of the TMDs is assumed to be a Gaussian. Although very simple, this approximation leads to a successful description of many sets of data

(see for instance Refs. [7–17]). However, as the quality and the amount of data has significantly improved lately, a more detailed picture of the partonic description is now becoming more and more necessary. In particular, the latest COMPASS analysis [18] of the SIDIS unpolarized cross section suggests that the average transverse momentum of the detected hadrons could sensitively depend on the parton momentum fractions x_B and z_h and even on flavor, although similar conclusions cannot be presently inferred from HERMES [19, 20] and JLAB data [21], as we will discuss in more details in Section III A. In Ref. [9], a simple Gaussian model was used to successfully describe the Cahn $\cos\phi_h$ azimuthal modulation measured by the EMC Collaboration [22] and allowed the extraction of the unpolarized TMD's Gaussian widths. Later, it has been realized that the predictions of Ref. [9] largely overestimated the more recent data from HERMES [23] and COMPASS [24] which have meanwhile become available. On the contrary, a large Cahn effect now seems to be required in order to describe the $\cos 2\phi_h$ asymmetries [25], at least at the COMPASS kinematics. Furthermore, a global phenomenological analysis of data led by Schweitzer, Teckentrup and Metz [15] suggests that the average transverse momenta $\langle k_\perp^2 \rangle$, used as a free parameter in the Gaussian, depends on $\sqrt{s}$, the center of mass energy of the target and the incoming lepton.

This complex scenario thus requires an accurate critical analysis of the work done so far, to try and shed some light on these apparent controversies. The detailed study of the COMPASS Collaboration on the P_T distribution of their SIDIS measurements [18], pointing to a considerable deviation from the expected behavior, prompted us to a reanalysis of the approximations used in our $k_\perp$ integration. In this paper, we examine the kinematical regions where order $\mathcal{O}(k_\perp^2/Q^2)$ and higher can be safely neglected and we realize that not all the kinematical domains of the existing and planned experiments satisfy the basic criteria $k_\perp \simeq P_T \simeq \Lambda_{QCD} \ll Q$. Inspired by the parton model, and still adopting a Gaussian model for our TMDs, we bound the integration range of transverse momenta $k_\perp$ and we observe, in some kinematical regions, remarkable deviations from the predictions obtained from the common TMD approach, based on the Gaussian parametrization integrated over the full $k_\perp$ range, $[0, \infty]$. We show that some kinematical ranges, typically low x_B or equivalently low Q^2 regions, are not safely controlled by the present phenomenological model, while bounds on $k_\perp$ can prevent uncontrolled large $k_\perp/Q$ contributions. This leads, for instance, to a better description of some observables like the $\langle \cos\phi_h \rangle$ asymmetry and introduces some interesting effects in the $\langle P_T^2 \rangle$ behaviors. However, simple parton model considerations are not sufficient to fully describe the present, in some sense puzzling, data: soft gluon emissions, higher twist contributions and QCD evolution of the TMDs can play a role.

Higher order contributions to cross sections and asymmetries are difficult to estimate; here, we will consider only those coming from purely kinematical corrections to twist-2 TMDs and show that they are not negligible in most of the present experimental setups. This makes the extraction of twist-3 TMDs from existing data troublesome.

Future experimental data from an Electron Ion Collider [26, 27], where the Q^2 range would be easily adjustable in order to estimate higher order contributions, will definitely help to disentangle them from leading twist contributions.

I. SIDIS KINEMATICS

Let us give a brief review of $\ell p \to \ell' h + X$ Semi-Inclusive Deep Inelastic Scattering kinematics. We study the SIDIS process in the $\gamma^* - p$ c.m. frame, where γ^* denotes the virtual photon. Following the Trento conventions [28], we take the virtual photon momentum q along the $+\hat{z}$ direction and the proton momentum P in the opposite direction, as shown in Fig. 1. The leptonic momenta define a plane that coincides with our $\hat{x}$-$\hat{z}$ plane. The detected hadron has momentum P_h, its transverse component is denoted by $\boldsymbol{P}_T$ and ϕ_h is its azimuthal angle: together with $\hat{z}$ they identify the hadron production plane, Fig. 1. We adopt the usual SIDIS variables neglecting the lepton, the proton and the final hadron masses:

$$
\begin{aligned}
s = (P+\ell)^2 \qquad Q^2 = -q^2 \qquad (P+q)^2 = W^2 \simeq \frac{1-x_B}{x_B}\, Q^2 \\
x_B = \frac{Q^2}{2P\cdot q} \simeq \frac{Q^2}{W^2+Q^2} \qquad y = \frac{P\cdot q}{P\cdot \ell} \simeq \frac{Q^2}{x_B s} \qquad z_h = (P\cdot P_h)/(P\cdot q)\ ,
\end{aligned}
\tag{1}
$$

where ℓ is the incoming lepton momentum. The proton and the virtual photon momenta can be written in the $\gamma^* - p$ c.m. frame, as functions of the invariants W and Q in this way:

$$
q = \frac{1}{2}\left(W - \frac{Q^2}{W}, 0, 0, W + \frac{Q^2}{W}\right) \qquad P = P_0(1,0,0,-1) \qquad P_0 = \frac{1}{2}\left(W + \frac{Q^2}{W}\right)\cdot
\tag{2}
$$

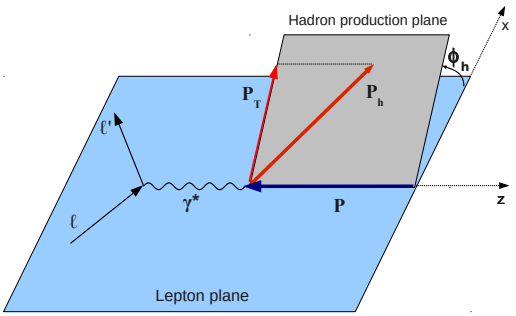

FIG. 1: Kinematical configuration and conventions for SIDIS processes in the $\gamma^* - p$ c.m. frame. The initial and final lepton momenta define the $\hat{x}$-$\hat{z}$ plane, while the detected hadron momentum and the $\hat{z}$ axis determine the hadron production plane, at an angle ϕ_h.

In the parton model the virtual photon scatters off a on-shell quark. The quark momentum k can be written, in the $\gamma^* - p$ c.m. as:

$$k = \left(xP_0 + \frac{k_\perp^2}{4xP_0}, \boldsymbol{k}_\perp, -xP_0 + \frac{k_\perp^2}{4xP_0} \right) \tag{3}$$

$$\tag{4}$$

where $x = k^-/P^-$ is the quark light-cone momentum fraction (see Appendix A for more details) and $\boldsymbol{k}_\perp$ is the quark intrinsic transverse momentum, see Fig. 2. The final emitted quark has momentum $k' = q + k$. Its on-shell condition

$$k'^2 = 2q \cdot k - Q^2 = 0 \tag{5}$$

implies [7]

$$x = \frac{1}{2} x_B \left(1 + \sqrt{1 + \frac{4k_\perp^2}{Q^2}} \right) . \tag{6}$$

As indicated in Fig. 2, $\boldsymbol{p}_\perp = \boldsymbol{P}_h - (\boldsymbol{P}_h \cdot \hat{\boldsymbol{k}}')\hat{\boldsymbol{k}}'$ is the transverse momentum of the hadron h *with respect to the direction* $\boldsymbol{k}'$ of the fragmenting quark, while $z = P_h^+/k'^+$ is the light-cone fraction of the quark momentum carried by the resulting hadron. The fragmenting variables z and $\boldsymbol{p}_\perp$ can be expressed in terms of the usual observed hadronic variables $\boldsymbol{P}_T$ and z_h, as shown in Eqs. (26) and (28) of Ref. [7].

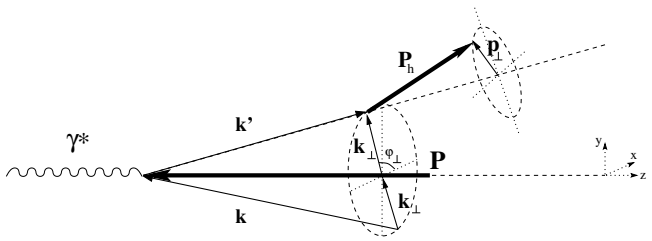

FIG. 2: Kinematical configuration and conventions for the SIDIS partonic sub-process: $\boldsymbol{k}$ and $\boldsymbol{k}'$ are the initial and final quark momenta, and $\boldsymbol{k}_\perp$ is their transverse component. P_h is the final, detected hadron momentum, with a $\boldsymbol{p}_\perp$ component, transverse with respect to the fragmenting quark direction $\boldsymbol{k}'$.

All the kinematical relations given above are exact expressions at all orders in a $(k_\perp/Q)$ expansion. Neglecting terms of order $\mathcal{O}(k_\perp^2/Q^2)$, they considerably simplify and we find:

$$x \simeq x_B\,, \qquad z \simeq z_h \qquad \boldsymbol{p}_\perp \simeq \boldsymbol{P}_T - z_h \boldsymbol{k}_\perp\,. \tag{7}$$

Transverse Momentum Dependent distributions depend on the kinematical variables x and $k_\perp$ defined above. Let's consider, for instance, the unpolarized distribution function $f_{q/p}(x, k_\perp)$, which gives the number density of unpolarized quarks inside an unpolarized proton; this function is usually normalized in such a way that

$$\int d^2k_\perp\, f_{q/p}(x, k_\perp) = f_{q/p}(x)\,, \tag{8}$$

where $f_{q/p}(x)$ is the usual, collinear parton distribution function at some given scale Q^2. The same logic holds for the unpolarized TMD fragmentation function, $D_{h/q}(z, p_\perp)$.

Very often, in phenomenological analysis, a Gaussian dependence of the TMDs is assumed, adopting the following parametrizations:

$$f_{q/p}(x, k_\perp) = f_{q/p}(x)\,\frac{1}{\pi\langle k_\perp^2\rangle}\,e^{-k_\perp^2/\langle k_\perp^2\rangle} \tag{9}$$

and

$$D_{h/q}(z, p_\perp) = D_{h/q}(z)\,\frac{1}{\pi\langle p_\perp^2\rangle}\,e^{-p_\perp^2/\langle p_\perp^2\rangle}\,, \tag{10}$$

where $f_{q/p}(x)$ and $D_{h/q}(z)$ can be taken from the available fits of world data, while $\langle k_\perp^2\rangle$ and $\langle p_\perp^2\rangle$ are free parameters to be extracted from dedicated fits.

Note that the functions defined in Eqs. (9) and (10) obey the normalization condition of Eq. (8), so that

$$\int_0^{2\pi} d\varphi \int_0^\infty dk_\perp\, k_\perp\, f_{q/p}(x, k_\perp) = f_{q/p}(x)\,. \tag{11}$$

The Gaussian parametrization in principle allows any value of $k_\perp$ from zero to infinity. However, the integrand is weighted by the Gaussian $k_\perp$ distribution, so that $k_\perp$ values larger than the Gaussian width, $\langle k_\perp^2\rangle$, are strongly suppressed. Typical values of $\langle k_\perp^2\rangle$ are of a few hundreds MeV. Thus if Q^2 is large with respect to $\langle k_\perp^2\rangle$, the Gaussian represents an effective model that prevents large $k_\perp/Q$ contributions to the cross section. However in many low energy SIDIS experiments, like HERMES and COMPASS, $\langle Q^2\rangle \simeq 2$ GeV^2 and the experimental cut $Q^2 > 1$ GeV^2 is used: thus at low x we have $Q^2 \simeq 1$ GeV^2. Therefore, in these particular cases, the Gaussian smearing is not sufficient to cut away large $k_\perp/Q$ contributions. Notice that these considerations are still valid for any phenomenological parametrization that does not impose any cut to the range of allowed $k_\perp$ values. Hence the necessity to explore whether it is possible to find a physical picture that allows us to put some further constraints on the partonic intrinsic motion.

II. PHYSICAL PARTONIC CUTS

In order to find some constraints on the partonic intrinsic motion, we adopt the simple picture of nucleons provided by the parton model. Although "non-physical" in many aspects, the parton model can be seen as good approximation and a toy–model to understand some physical QCD features. In particular, it gives kinematical limits on the transverse momentum size, which can be obtained by requiring the energy of the parton to be less than the energy of the parent hadron and by preventing the parton to move backward with respect to the parent hadron direction ($k_z < 0$). The energy bound implies:

$$\begin{aligned} xP_0 + \frac{k_\perp^2}{4xP_0} \le P_0 \;&\Rightarrow\; k_\perp^2 \le 4x(1-x)P_0^2 \\ &\Rightarrow\; k_\perp^2 \le \frac{x(1-x)}{x_B(1-x_B)}Q^2\,. \end{aligned} \tag{12}$$

Inserting Eq. (6) in Eq. (12) and solving one finds:

$$k_\perp^2 \le (2-x_{_B})(1-x_{_B})Q^2 \quad,\quad 0 < x_{_B} < 1\,. \tag{13}$$

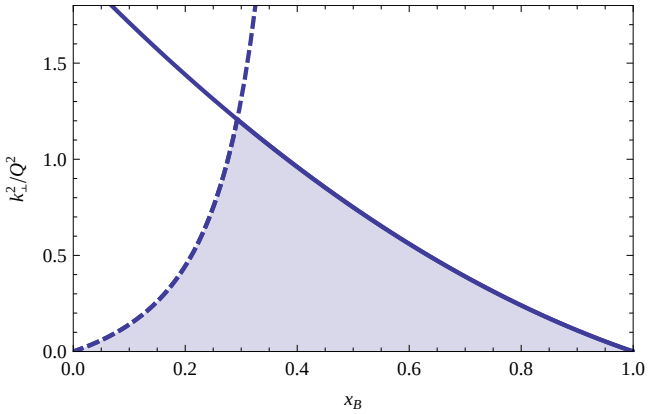

FIG. 3: $k_\perp^2/Q^2$ phase space as determined by the bounds of Eqs. (13) and (15). The allowed region, which fulfills both bounds, is represented by the shaded area below the solid line, corresponding to Eq. (13) and the dashed line, corresponding to Eq. (15). Notice that present data from HERMES and COMPASS experiments span the region $x_B \lesssim 0.3$, where only the momentum bound of Eq. (15) plays a role.

Requiring the parton to move in the forward direction with respect to the parent hadron gives:

$$\begin{aligned}(\boldsymbol{P}\cdot\boldsymbol{k}) > 0 \;&\Rightarrow\; k_\perp^2 \le 4x^2P_0^2 \\ &\Rightarrow\; k_\perp^2 \le \frac{x^2}{x_B(1-x_B)}Q^2\,. \end{aligned} \tag{14}$$

Using Eq. (6) and solving we find

$$k_\perp^2 \le \frac{x_B(1-x_B)}{(1-2x_B)^2}Q^2\;,\; x_B < 0.5\,. \tag{15}$$

Notice that these are exact relations, which hold at all orders in $(k_\perp/Q)$. These constraints are obtained assuming that partons are on-shell (the parton off-shellness should be very small, at least in the region where we will apply the parton model).

The ratio $k_\perp^2/Q^2$, as constrained by Eqs. (13) and (15), is shown in Fig. 3 as a functions of x_B: from this plot it is immediately evident that although in principle Eq. (15) (represented by the dashed line) gives a stringent limit on $k_\perp^2/Q^2$ in the region $x_B < 0.5$, it intercepts the bound of Eq. (13) (solid line) in $x_B \simeq 0.3$, where the latter becomes most relevant. Notice also that present data from HERMES and COMPASS experiments span the region $x_B \lesssim 0.3$, where only the momentum bound of Eq. (15) plays a role.

Once the maximum value of $k_\perp$ is bounded by the conditions of Eqs. (13) and (15), to comply with the normalization condition of Eq. (8), we set the right normalization coefficient

$$f_{q/p}(x,k_\perp) = f_{q/p}(x)\,\frac{1}{1-e^{-(k_\perp^{\max})^2/\langle k_\perp^2\rangle}}\,\frac{e^{-k_\perp^2/\langle k_\perp^2\rangle}}{\pi\langle k_\perp^2\rangle}\,, \tag{16}$$

where $(k_\perp^{\max})^2$ denotes the maximum value of $k_\perp^2$ for each given values of x_B and Q^2 as required by Eqs. (13),(15), so that

$$f_{q/p}(x) = \int_0^{2\pi} d\varphi \int_0^{k_\perp^{\max}} k_\perp\, dk_\perp\, f_{q/p}(x,k_\perp)\,. \tag{17}$$

This normalization will allow us to reproduce correctly all inclusive cross-sections, such as the DIS cross-section, for which collinear results are known. Note that if $Q \to \infty$ then $k_\perp^{max} \to \infty$ and one obtains the usual normalization of Eq. (8).

III. UNPOLARISED SIDIS CROSS SECTION

According to Refs. [1–3] the unpolarized differential cross section for the SIDIS process, $\ell + p \to \ell' h X$ can be written as

$$\frac{d\sigma^{\ell+p\to\ell' hX}}{dx_{_B}\, dy\, dz_h\, d^2\boldsymbol{P}_T} = \frac{4\pi\,\alpha^2}{x_{_B} s y^2}\left\{\frac{1+(1-y)^2}{2}F_{UU} + (2-y)\sqrt{1-y}\,\cos\phi_h\, F_{UU}^{\cos\phi_h} + (1-y)\,\cos 2\phi_h\, F_{UU}^{\cos 2\phi_h}\right\}, \quad (18)$$

where the F "structure functions", which involve the relevant convolutions of distribution and fragmentation functions over the intrinsic transverse momenta, are defined within a TMD factorization scheme, at order $\mathcal{O}(k_\perp/Q)$, as

$$F_{UU} = \sum_q e_q^2 \int d^2\boldsymbol{k}_\perp\, f_{q/p}(x,k_\perp)\, D_{h/q}(z,p_\perp)\,, \quad (19)$$

$$F_{UU}^{\cos\phi_h} = 2\sum_q e_q^2 \int d^2\boldsymbol{k}_\perp\, \frac{k_\perp}{Q}\left[(\hat{\boldsymbol{P}}_T\cdot\hat{\boldsymbol{k}}_\perp)\, f_{q/p}(x,k_\perp)\, D_{h/q}(z,p_\perp) + \frac{P_T - z_h k_\perp\,(\hat{\boldsymbol{P}}_T\cdot\hat{\boldsymbol{k}}_\perp)}{2p_\perp}\,\Delta f_{q^\uparrow/p}(x,k_\perp)\,\Delta^N D_{h/q^\uparrow}(z,p_\perp)\right], \quad (20)$$

$$F_{UU}^{\cos 2\phi_h} = -\sum_q e_q^2 \int d^2\boldsymbol{k}_\perp \left[\frac{P_T\,(\hat{\boldsymbol{P}}_T\cdot\hat{\boldsymbol{k}}_\perp) - 2z_h k_\perp(\hat{\boldsymbol{P}}_T\cdot\hat{\boldsymbol{k}}_\perp)^2 + z_h k_\perp}{2p_\perp}\right]\Delta f_{q^\uparrow/p}(x,k_\perp)\,\Delta^N D_{h/q^\uparrow}(z,p_\perp)\,. \quad (21)$$

Although three different azimuthal modulations are simultaneously at work in the total unpolarized SIDIS cross section of Eq. (18), to extract single effects one can introduce the following azimuthal moments

$$\langle\cos\phi_h\rangle = \frac{\int d\phi_h\, d\sigma^{\ell p\to\ell' hX}\,\cos\phi_h}{\int d\phi_h\, d\sigma^{\ell p\to\ell' hX}}\,, \qquad \langle\cos 2\phi_h\rangle = \frac{\int d\phi_h\, d\sigma^{\ell p\to\ell' hX}\,\cos 2\phi_h}{\int d\phi_h\, d\sigma^{\ell p\to\ell' hX}}\,, \quad (22)$$

which isolate the contributions of $F_{UU}^{\cos\phi_h}$ and $F_{UU}^{\cos 2\phi_h}$ from the traditional, collinear term F_{UU}. As we showed in Ref. [3], the F structure functions in Eqs. (19), (20) and (21) coincide with those defined in Ref. [2], considering only leading twist TMDs. In the phenomenological study we will perform in what follows, we will not consider higher twist dynamical contributions [2] to the structure functions, therefore we shall keep in mind that strong deviations of measured quantities from the predictions obtained in this simple model will signal the presence of higher twist contributions.

In Eqs. (19) and (20), $f_q(x,k_\perp)$ is the unpolarized TMD distribution function and $D_q^h(z,p_\perp)$ is the unpolarised TMD fragmentation function discussed in Section I, while $\Delta f_{q^\uparrow/p}(x,k_\perp)$ is the Boer-Mulders distribution function, related to the number density of transversely polarized quarks inside an unpolarized proton, and $\Delta^N D_{h/q^\uparrow}(z,p_\perp)$ is the Collins fragmentation function which, in turn, is related to the number density of transversely polarized quarks fragmenting into a spinless hadron. Other common notations used for the Boer-Mulders and Collins functions are:

$$\Delta f_{q^\uparrow/p}(x,k_\perp) = -\frac{k_\perp}{M}\, h_1^\perp(x,k_\perp)\,, \quad (23)$$

$$\Delta^N D_{h/q^\uparrow}(z,p_\perp) = \frac{2p_\perp}{zM_h} H_1^\perp(z,p_\perp)\,, \quad (24)$$

where M and M_h are the masses of the initial proton and of the final hadron, respectively.

Summarizing, Eq. (19) corresponds to the usual, collinear $f_{q/p}\otimes D_{h/q}$ contribution to the unpolarized SIDIS cross section; in the $\cos\phi_h$ azimuthal modulation of Eq. (20) the first term is the Cahn effect [4, 5], signaling the existence of transverse momenta in the partonic scattering even when considering only unpolarized partons, while the second term corresponds to the Boer-Mulders $\otimes$ Collins contribution of transversely polarized quarks to the unpolarized cross section; finally, Eq. (21) gives the $\cos 2\phi_h$ azimuthal modulation of the unpolarized SIDIS cross section. An additional contribution to the $\cos\phi_h$ modulation can be generated by "dynamical" higher twist contributions from twist-3 functions [2]. Instead, the $\cos 2\phi_h$ azimuthal moment in Eq. (21) is not suppressed by $1/Q$ and does not receive any dynamical or kinematical twist-3 contribution [2], but can be affected by twist-4 contributions, like the $\cos 2\phi_h$ Cahn effect discussed in Section III C.

Therefore from this azimuthal moment one could extract the Boer-Mulders and Collins TMD's, in all those kinematical ranges in which higher orders in the $k_\perp/Q$ expansion can safely be neglected. As a matter of facts, as we will see in Section II, higher orders of $(k_\perp/Q)^n$, $n \geq 2$, could potentially be important when analysing HERMES, COMPASS and JLab experimental data, and should not be neglected. Therefore twist-4 contributions could be important in these kinematics. One of these contributions, the "twist-4" Cahn effect, Eq.(35), has been analyzed phenomenologically in Ref [25], see Section III C.

For the Boer-Mulders and Collins functions, we assume parametrizations similar to those in Eqs. (9) and (10), with an extra multiplicative factor $k_\perp$ or $p_\perp$, respectively, to give them the appropriate behavior in the small $k_\perp$ or $p_\perp$ region [3, 12]:

$$\Delta f_{q^\uparrow/p}(x,k_\perp) \;=\; \Delta f_{q^\uparrow/p}(x)\,\sqrt{2e}\,\frac{k_\perp}{M_{BM}}\,\frac{e^{-k_\perp^2/\langle k_\perp^2\rangle_{BM}}}{\pi\langle k_\perp^2\rangle}\,, \tag{25}$$

$$\Delta^N D_{h/q^\uparrow}(z,p_\perp) \;=\; \Delta^N D_{h/q^\uparrow}(z)\,\sqrt{2e}\,\frac{p_\perp}{M_h}\,\frac{e^{-p_\perp^2/\langle p_\perp^2\rangle_C}}{\pi\langle p_\perp^2\rangle}\,, \tag{26}$$

with

$$\langle k_\perp^2\rangle_{BM} = \frac{\langle k_\perp^2\rangle\, M_{BM}^2}{\langle k_\perp^2\rangle + M_{BM}^2}\,, \qquad \langle p_\perp^2\rangle_C = \frac{\langle p_\perp^2\rangle\, M_h^2}{\langle p_\perp^2\rangle + M_h^2}\,. \tag{27}$$

The x-dependent function $\Delta f_{q^\uparrow/p}(x)$ and the z-dependent function $\Delta^N D_{h/q^\uparrow}(z)$ in Eqs. (25) and (26) are not known, and should be determined phenomenologically by fitting the available data on azimuthal asymmetries and moments; the $k_\perp$ and $p_\perp$ dependent terms and their normalization are chosen in such a way that positivity bounds [29] are fulfilled automatically.

At this stage, the usual procedure would be to perform an analytical $k_\perp$ integration of Eqs. (19-21) over the range $[0,\infty]$, using the parametrizations in Eqs. (9), (10), (25) and (26) with the appropriate normalization of Eq. (8), and to re-express all the F structure functions in terms of the Gaussian parameters:

$$F_{UU} \;=\; \sum_q e_q^2\, f_{q/p}(x_B)\, D_{h/q}(z_h)\frac{e^{-P_T^2/\langle P_T^2\rangle_G}}{\pi\langle P_T^2\rangle_G} \tag{28}$$

$$F_{UU}^{\cos 2\phi_h} \;=\; -e\,P_T^2 \sum_q e_q^2\,\frac{\Delta f_{q^\uparrow/p}(x_B)}{M_{BM}}\,\frac{\Delta^N D_{h/q^\uparrow}(z_h)}{M_h}\,\frac{e^{-P_T^2/\langle P_T^2\rangle_{BM}}}{\pi\langle P_T^2\rangle_{BM}^3}\,\frac{z_h\,\langle k_\perp^2\rangle_{BM}^2\langle p_\perp^2\rangle_C^2}{\langle k_\perp^2\rangle\langle p_\perp^2\rangle} \tag{29}$$

$$\begin{aligned} F_{UU}^{\cos\phi_h} \;=\; & -2\,\frac{P_T}{Q}\sum_q e_q^2\, f_{q/p}(x_B)\, D_{h/q}(z_h)\,\frac{e^{-P_T^2/\langle P_T^2\rangle_G}}{\pi\langle P_T^2\rangle_G^2}\, z_h\langle k_\perp^2\rangle \\ & +2e\,\frac{P_T}{Q}\sum_q e_q^2\,\frac{\Delta f_{q^\uparrow/p}(x_B)}{M_{BM}}\,\frac{\Delta^N D_{h/q^\uparrow}(z_h)}{M_h}\,\frac{e^{-P_T^2/\langle P_T^2\rangle_{BM}}}{\pi\langle P_T^2\rangle_{BM}^4} \\ & \times\frac{\langle k_\perp^2\rangle_{BM}^2\langle p_\perp^2\rangle_C^2}{\langle k_\perp^2\rangle\langle p_\perp^2\rangle}\Big[z_h^2\langle k_\perp^2\rangle_{BM}\Big(P_T^2-\langle P_T^2\rangle_{BM}\Big)+\langle p_\perp^2\rangle_C\langle P_T^2\rangle_{BM}\Big]\,, \end{aligned} \tag{30}$$

where

$$\langle P_T^2\rangle_G = \langle p_\perp^2\rangle + z_h^2\langle k_\perp^2\rangle\,, \tag{31}$$

$$\langle P_T^2\rangle_{BM} = \langle p_\perp^2\rangle_C + z_h^2\langle k_\perp^2\rangle_{BM}\,. \tag{32}$$

We stress that the analytical integration which leads to Eqs. (28)–(30) is performed over the full range of $\boldsymbol{k}_\perp$ values:

$$\int d^2\boldsymbol{k}_\perp \Rightarrow \int_0^{2\pi} d\varphi \int_0^\infty dk_\perp\, k_\perp\,, \tag{33}$$

and that the expressions (31) and (32) which relate the $\langle P_T^2\rangle$ to $\langle p_\perp^2\rangle$, $\langle k_\perp^2\rangle$ and z_h are due to such choice. In other words, Eqs. (31) and (32) are a direct consequence not only of the assumption of Gaussian $k_\perp$ and $p_\perp$ distributions of the TMDs, but also of the choice of the $k_\perp$ integration range. Many phenomenological analysis

on the TMDs are based on the Gaussian assumption and overlook any issue regarding the limits of integration over $k_\perp$. However, great attention to this should be payed when analysing data from JLAB, HERMES and COMPASS experiments, where the average Q^2 is not so large (~ 2 GeV^2). Therefore in some kinematical ranges it could happen that the $(k_\perp/Q)$ values accessed are not small. One immediately visible signal of this is the Cahn effect in both azimuthal moments, at twist-3 in $\langle \cos\phi_h \rangle$ and at twist-4 in $\langle \cos 2\phi_h \rangle$, which are directly proportional to $k_\perp/Q$ and $k_\perp^2/Q^2$ respectively, and are found to be (phenomenologically) large.

A. Impact of the partonic cuts on the F_{UU} term of the unpolarized cross section and on $\langle P_T^2 \rangle$

In this section we will show the impact of the $k_\perp$ cuts presented in Eqs. (13) and (15) on the calculation of the SIDIS unpolarized cross section and on the average transverse momenta of the final detected hadron, $\langle P_T^2 \rangle$. Figure 4 shows the first term of the SIDIS unpolarized cross section, proportional to F_{UU}, calculated for HERMES and COMPASS kinematics (the detailed experimental cuts are reported in Appendix B) for π^+ production, integrated over all variables but one, x_B, z_h and $\boldsymbol{P}_T$.

We use the unpolarized integrated PDF's given in Ref. [30] and the unpolarized fragmentation functions of Ref. [31]. For the Gaussian widths of the unpolarized distribution and fragmention TMDs we use the values extracted in Ref. [7]: $\langle k_\perp^2 \rangle = 0.25$ GeV^2 and $\langle p_\perp^2 \rangle = 0.20$ GeV^2. The solid (red) line, denoted in the legend as "*num+cuts*", corresponds to the unpolarized cross section calculated according to Eqs. (18), (19)–(21) with a numerical $k_\perp$ integration over the range obtained implementing the $k_\perp$-cuts of Eqs. (13) and (15). The dashed (blue) line, indicated as "*analyt*", is the unpolarized cross section calculated according to Eqs. (28)–(30), resulting from a $k_\perp$ analytical integration over the range $[0, \infty]$. These plots clearly show that, as far as the x_B and z_h distributions are concerned, there is no difference between the two calculations. Instead, a slight modification can be observed in the P_T distribution (see the upper and lower right panels).

The average hadronic transverse momentum $\langle P_T^2 \rangle$ of the final, detected hadron h is defined as:

$$\langle P_T^2 \rangle = \frac{\int d^2\boldsymbol{P}_T P_T^2 d\sigma}{\int d^2\boldsymbol{P}_T d\sigma} \,. \tag{34}$$

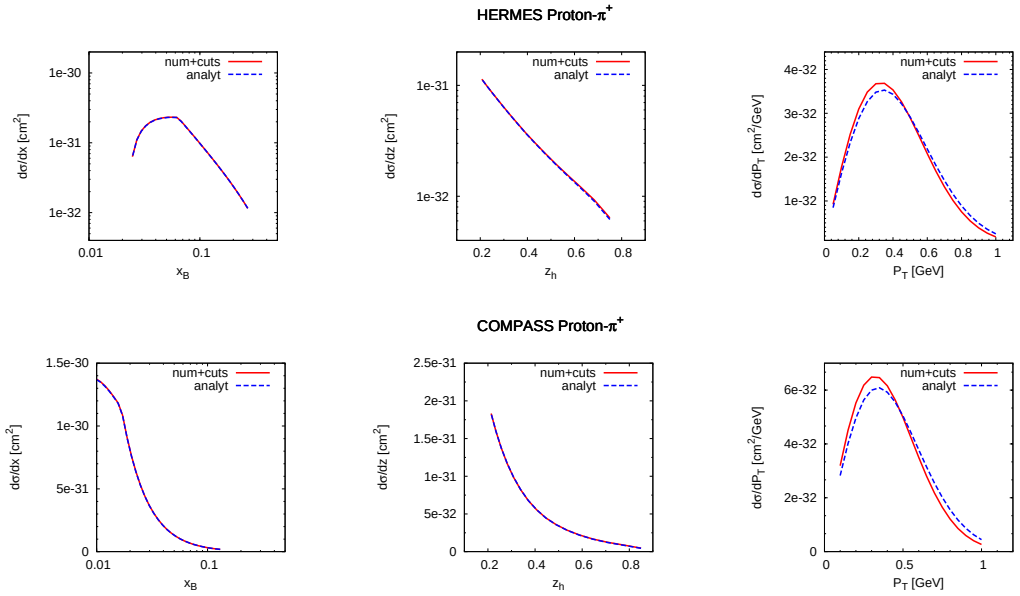

FIG. 4: Unpolarized cross section for π^+ production at HERMES (upper panel) and COMPASS experiment on a proton target (lower panel), as a function of x_B (left plot), z_h (central plot) and P_T (right plot). The (red) solid line corresponds to the unpolarized cross section calculated according to Eq. (18) with a numerical $k_\perp$ integration implementing the $k_\perp$-cuts of Eqs. (13) and (15). The dashed (blue) line is the unpolarized cross section calculated according to Eqs. (28)–(30) resulting from an analytical $k_\perp$ integration from zero to infinity. We do not show the analogous cross section corresponding to the COMPASS experiment on deuteron target as the effects of the $k_\perp$ cuts are very similar to those for COMPASS on proton target.

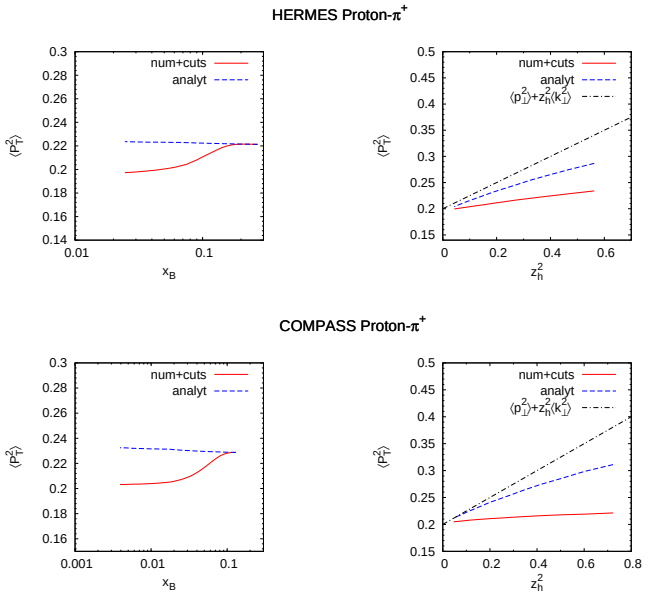

FIG. 5: $\langle P_T^2\rangle$, defined in Eq. (34), as a function of x_B (left plot) and of z_h^2 (right plot), for π^+ production at HERMES (upper panel) and COMPASS (lower panel). The solid (red) line corresponds to $\langle P_T^2\rangle$ calculated with a numerical integration implementing Eqs. (13) and (15), while the dashed (blue) line is $\langle P_T^2\rangle$ calculated with an analytical integration. In both cases we have applied the experimental cuts on P_T reported in Appendix B . Finally, the dash-dotted (black) line corresponds to the Gaussian $\langle P_T^2\rangle_G$.

Notice that if the integral in Eq. (34) is performed over the range $[0,\infty]$, then $\langle P_T^2\rangle$ coincides with the Gaussian width of the unpolarized P_T distribution of Eq. (28): $\langle P_T^2\rangle \equiv \langle P_T^2\rangle_G$. The experimental P_T range, however, usually span a finite region between some P_T^{min} and P_T^{max}; therefore, in any experimental analysis, one inevitably has $\langle P_T^2\rangle \neq \langle P_T^2\rangle_G$, even without considering the cuts in Eqs. (13) and (15). Consequently, the relation $\langle P_T^2\rangle \simeq \langle p_\perp^2\rangle + z_h^2\langle k_\perp^2\rangle$ holds only approximatively.

Figure 5 shows the average hadronic transverse momentum $\langle P_T^2\rangle$ as a function of x_B and of z_h^2 for π^+ at HERMES and COMPASS, respectively. The solid (red) lines correspond to $\langle P_T^2\rangle$ calculated according to Eq. (18) with a numerical $k_\perp$ integrations and implementing Eqs. (13) and (15). Instead, the dashed (blue) lines correspond to $\langle P_T^2\rangle$ calculated according to Eqs. (28)–(30) with an analytical integration. In both cases we have taken into account the appropriate experimental cuts on P_T reported in Appendix B. Clearly, at low x, there is a substantial deviation from the analytical calculation, which also affects the value of $\langle P_T^2\rangle$ as a function of z_h^2. As far as the z_h dependence is concerned, first of all, one can see that there is a large deviation from the naive formula, Eq. (31), corresponding to the dash-dotted (black) lines, for both calculations. Secondly, although the z_h^2-dependence is not linear any more, it seems to be approaching an almost constant behavior (as opposed to what COMPASS latest analysis [18] seems to indicate). Notice that, independently from Eqs. (13) and (15), if we naively assume $\langle P_T^2\rangle = \langle p_\perp^2\rangle + z_h\langle k_\perp^2\rangle$ in any analysis of the data we would conclude that the effective $\langle k_\perp^2\rangle$ is smaller than the value $\langle k_\perp^2\rangle = 0.25$ GeV^2 that we used as an input in the Gaussian. Also $\langle p_\perp^2\rangle \neq 0.20$ GeV^2, as a consequence of the limits of integration on P_T. Fig. 6 shows how the integration range influences the value of $\langle P_T^2\rangle$ when we integrate analytically (left plot) or implementing the cuts in Eqs. (13) and (15) (right plot).

Finally, different behaviors in x_B could, in principle, imply different values of $\langle P_T^2\rangle$ for π^+ and π^-. We have explored this possibility in order to account for the slight discrepancy in the $\langle P_T^2\rangle$ corresponding to π^+ and π^- as observed by COMPASS. Unfortunately the difference predicted by our model for π^+ and π^- is extremely tiny, even at COMPASS kinematics, as can be appreciated in Fig. 7. One should keep in mind that the tiny separation observed here occurs for purely kinematical effects, although larger differences between the π^+ and π^- average P_T could be generated by adopting different $k_\perp$ distribution widths for different quark flavours.

In Fig. 8 we show how a cut in Q^2 can change the description of data. We can see that cutting at higher Q^2 means cutting the lower x_B region, where the constraint of Eq. (15) strongly applies. As a consequence, if we apply high Q^2 cuts the description of the data with or without $k_\perp$-cuts is the same. This means that, provided Eqs. (13) and (15) are right, there is a region of x_B or Q^2 where we can safely assume that $(k_\perp/Q)$ corrections are small or negligible and where a phenomenological analysis is safe and unambiguous.

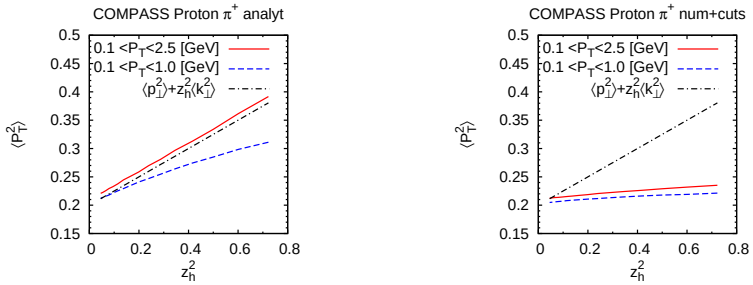

FIG. 6: $\langle P_T^2 \rangle$, at COMPASS kinematics as a function of z_h^2 for different ranges in P_T, calculated analytically (left plot) and numerically implementing Eqs. (13) and (15) (right plot).

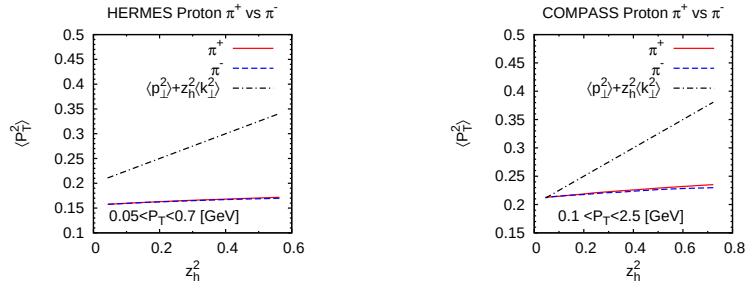

FIG. 7: $\langle P_T^2 \rangle$ as function of z_h^2 for π^+ and π^- production at HERMES (left plot) and COMPASS(right plot) pion production on a proton target.

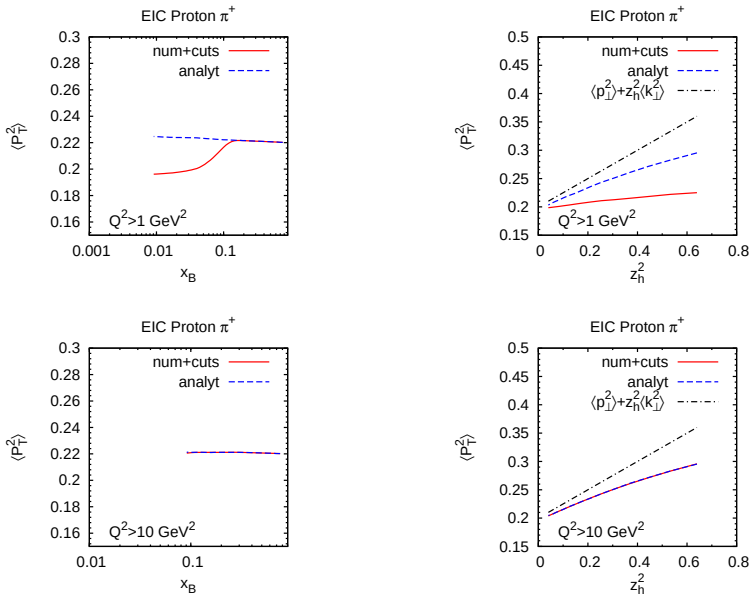

FIG. 8: $\langle P_T^2 \rangle$, defined in Eq. (34), as a function of x_B (left plot) and of z_h^2 (right plot), for π^+ production at EIC kinematics, with $Q^2 > 1$ GeV^2 cut (upper panel) and $Q^2 > 10$ GeV^2 cut (lower panel). The solid (red) line corresponds to $\langle P_T^2 \rangle$ calculated starting from Eq. (18) and then integrating it numerically, implementing Eqs. (13,15). The dashed (blue) line is $\langle P_T^2 \rangle$ calculated starting from Eqs. (28)–(30).

B. Impact of the partonic cuts on the azimuthal moment $\langle \cos\phi_h \rangle$

At this stage, we are ready to evaluate the effect of the physical partonic cuts on the $\langle \cos\phi_h \rangle$ and $\langle \cos 2\phi_h \rangle$ azimuthal moments, Eq. (22), which represent the most delicate terms of the SIDIS unpolarized cross section.

The $\langle \cos\phi_h \rangle$ modulation receives two contributions, both suppressed by one power of $(k_\perp/Q)$, see Eq. (20). The Cahn term, which is proportional to the convolution of the unpolarized distribution and fragmentation functions, was extensively studied in Ref. [7]. There, EMC measurements [22] on the $\cos\phi_h$ modulation and of the P_T distribution on the unpolarized SIDIS cross section were used to determine the Gaussian width of the $k_\perp$ distribution of the unpolarized distribution function $f_{q/p}(x, k_\perp)$. The second term is proportional to the convolution of the Boer-Mulders distribution function and the Collins fragmentation function and was neglected in Ref. [7]. Since then, new and higher statistics experimental data have become available [23, 24]: it is therefore timely and interesting to evaluate its net contribution to the $\langle \cos\phi_h \rangle$ azimuthal moment, using some reasonable estimate of the Boer-Mulders and Collins TMDs from the literature [13, 25].

Figure 9 shows how a large deviation from the analytical integration results is obtained by applying the $k_\perp$ bounds of Eqs. (13) and (15) when computing the Cahn effect contribution to $\langle \cos\phi_h \rangle$ corresponding to the HERMES and COMPASS kinematics, whereas for the EMC set up, see Fig. 11, one can hardly notice any difference. The reason is quite obvious: while EMC used high $Q^2 > 5$ GeV^2 cuts, HERMES and COMPASS experiments typically have $Q^2 > 1$ GeV^2.

In Fig. 9 our results, obtained with and without $k_\perp$ - cuts, are compared to the latest HERMES [23] and COMPASS [24] data. Although still showing a considerable deviation from the experimental data, our calculation confirms that physical partonic cuts have a quite dramatic effect in the small x region, and should therefore be taken into account in any further analysis of these experimental data.

To evaluate the influence of the partonic cuts on the contribution to $\langle \cos\phi_h \rangle$ originating from the Boer-Mulders$\otimes$Collins term, we use the parametrization of Ref. [32] for the Collins function while for the Boer-Mulders function we apply the extraction of Ref [25]. It can be seen from Fig. 10 that the Boer-Mulders contribution is very tiny (it gives a correction of a few percents over the dominant Cahn contribution) and is not strongly affected by kinematical cuts of Eqs. (13) and (15).

The residual discrepancy between the model prediction and the measurements of the $\langle \cos\phi_h \rangle$ azimuthal moment could indicate that higher twist contributions, from pure twist-3 functions, for example, might be non negligible in this modulation. More elaborated phenomenological studies including twist-3 TMDs would be necessary to confirm these observation.

C. Impact of the partonic cuts on the azimuthal moment $\langle \cos 2\phi_h \rangle$

The $\langle \cos 2\phi \rangle$ azimuthal modulation, at twist-2, consists of a term proportional to the Boer-Mulders$\otimes$ Collins, see Eq. (21). Although it is not affected by any twist-three corrections, in kinematical ranges where Q^2 is not very large compared to the average $k_\perp^2$, twist-4 contributions cannot be neglected. In particular, a twist-4 "Cahn-like" effect actually gives a large contribution to the $\langle \cos 2\phi \rangle$ azimuthal moment, as was explained in details in Ref. [25]. This provides an additional term to the $F_{UU}^{\cos 2\phi_h}$ structure function, Eq. (21), of the form

$$2 \sum_q e_q^2 \int d^2\boldsymbol{k}_\perp \frac{k_\perp^2}{Q^2} \left[2(\hat{\boldsymbol{P}}_T \cdot \hat{\boldsymbol{k}}_\perp)^2 - 1 \right] f_{q/p}(x, k_\perp)\, D_{h/q}(z, p_\perp)\,. \tag{35}$$

In Ref. [25], the presence of a twist-4 term proved to be crucial to understand the available experimental data from HERMES [33, 34] and COMPASS [35, 36] results. Here, a detailed study inspired by the fact that the HERMES P_T spectrum can be reproduced by Monte Carlo calculations with $\langle k_\perp^2 \rangle = 0.18$ GeV^2, pointed out that slightly different values of TMD widths might be required for different experiments.

We revisit these calculations by applying the physical cuts on the partonic transverse momenta, Eqs. (13) and (15), and find that the value of the twist-4 Cahn effect is very sensitive to the $k_\perp$ constraint, as it can be seen in the upper panels of Fig. 12, while the Boer-Mulders contribution does not exhibit such a strong dependence, as shown in the lower panels of Fig. 12. This is explained by the fact that, indeed, the accessed values of $(k_\perp^2/Q^2)$ are strongly suppressed by limiting the range of $k_\perp$. The sum of the Boer-Mulders and Cahn-like contributions which reproduces the $\langle \cos 2\phi_h \rangle$ azimuthal modulation is presented in Fig. 13. One can see that the description of the available data is very good. In Ref. [25] a satisfactory description of the HERMES data was achieved by adopting a smaller value of $\langle k_\perp^2 \rangle = 0.18$ GeV^2 for the HERMES data, while keeping $\langle k_\perp^2 \rangle = 0.25$ GeV^2 for fitting the COMPASS data (see FIT II). Here a similar improvement is achieved by taking into account the physical

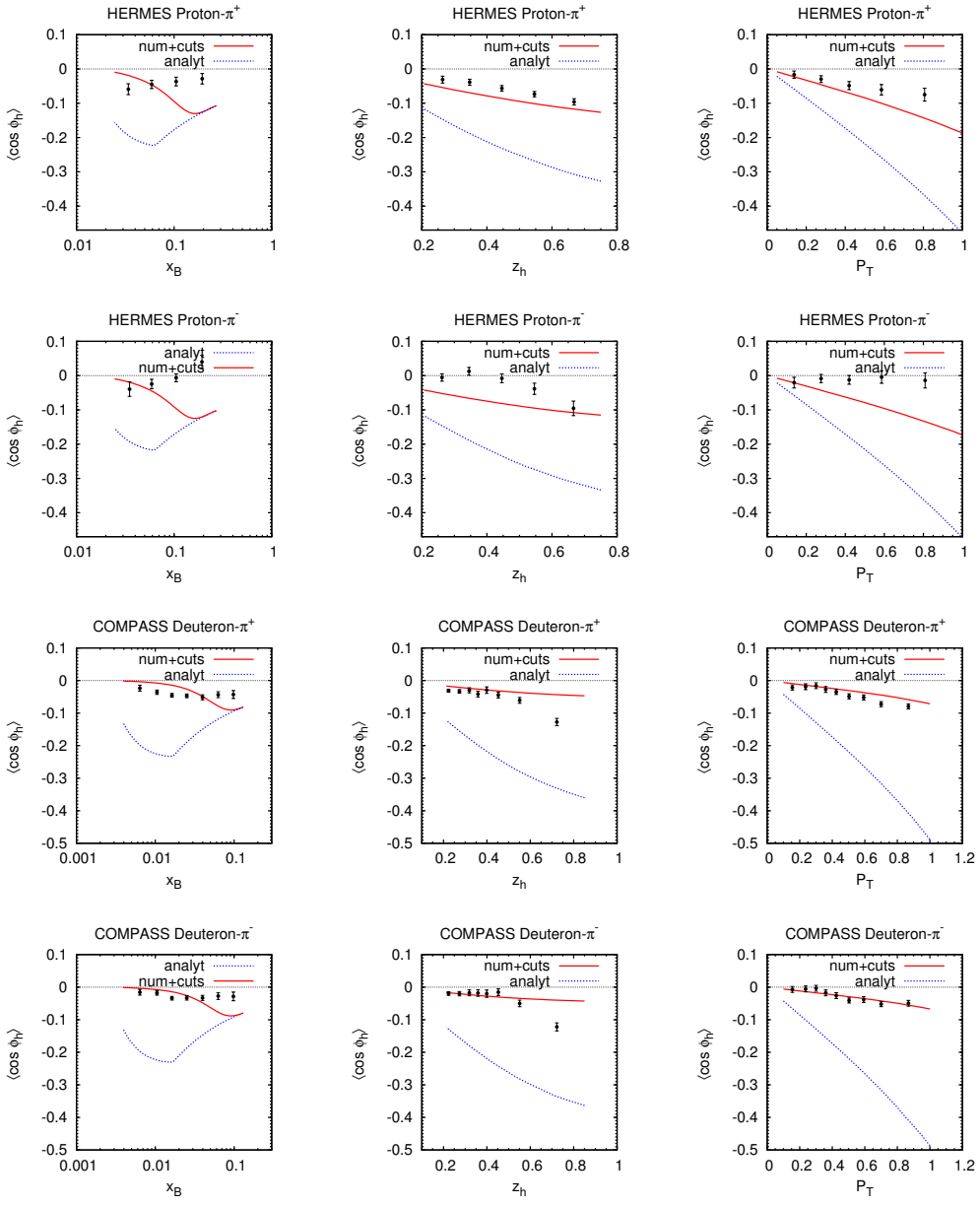

FIG. 9: Cahn contribution to $\langle \cos\phi_h \rangle$ for π^+ and π^- production at HERMES and COMPASS kinematics, as a function of x_B (left plot), z_h (central plot) and P_T (right plot). The solid (red) line corresponds to $\langle \cos\phi_h \rangle$ calculated according to Eq. (20) with a numerical $k_\perp$ integration over the range $[0, k_\perp^{max}]$. The dashed (blue) line is $\langle \cos\phi_h \rangle$ calculated according to Eq. (30) obtained by integrating over $k_\perp$ analytically. We do not show the Boer-Mulders contribution as it is negligible (see Fig. 10). The full circles are preliminary experimental data from HERMES [23] and COMPASS [24] Collaborations.

cuts on the partonic transverse momenta which, by cutting the range of allowed $k_\perp$ values, effectively reduces the average value of $k_\perp$ decreasing the contribution generated by the Cahn effect. Nevertheless, a slight puzzle still remains: while HERMES data seem to demand a very small Cahn contribution, it can be seen from the analysis in Ref. [25] and from Fig. 15 that COMPASS data seem to require a large Cahn contribution. Large Cahn contributions can only be generated by large $k_\perp$ values, as we have seen. Since the COMPASS target is not a pure Deuterium target, but a Li^6D target, possible nuclear effects can enhance the values of $k_\perp$. Partonic transverse motion generated by the nuclear smearing mechanisms does not have to fulfill the bounds in Eq. (13) and (15) and can be effectively simulated by a traditional Gaussian smearing, without any restriction. Future COMPASS data on pure hydrogen target will help our understanding.

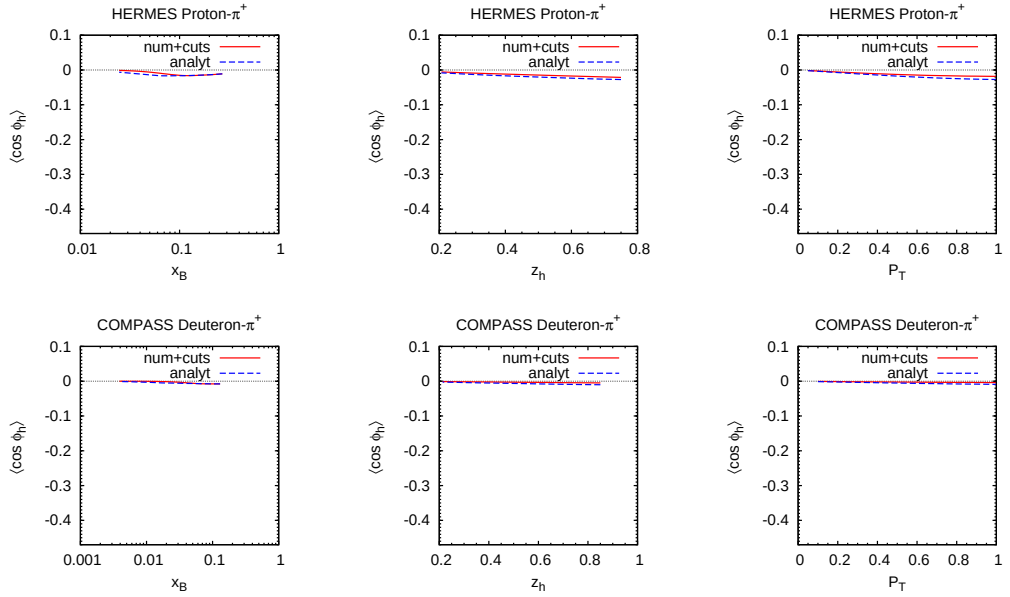

FIG. 10: Boer-Mulders contribution to the $\langle \cos\phi_h \rangle$ azimuthal modulation for π^+ and π^- production at the HERMES and COMPASS kinematics, as a function of x_B (left plot), z_h (central plot) and P_T (right plot). The solid (red) line corresponds to $\langle \cos\phi_h \rangle$ calculated according to Eq. (20) with a numerical $k_\perp$ integration over the range $[0, k_\perp^{max}]$ as given by Eqs. (13) and (15). The dashed (blue) line is $\langle \cos\phi_h \rangle$ calculated according to Eq. (30) obtained by integrating over $k_\perp$ analytically.

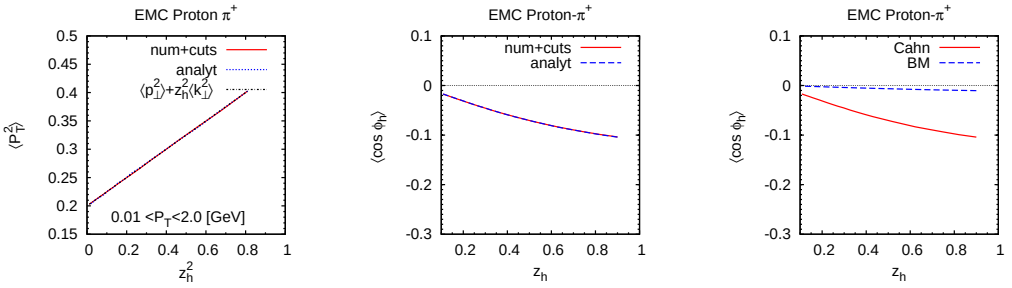

FIG. 11: On the left and the central plots, respectively, the $\langle P_T^2 \rangle$ and the $\langle \cos\phi_h \rangle$ azimuthal modulation for π^+ production at EMC. The solid (red) line corresponds to the calculation performed starting from Eq. (18) and then integrating it numerically, implementing Eqs. (13) and (15). The dashed (blue) line correspond to the analytical calculation. On the right plot the Cahn (red solid line) and the Boer-Mulder (blu dashed line) contributions to the $\langle \cos\phi_h \rangle$ azimuthal modulation.

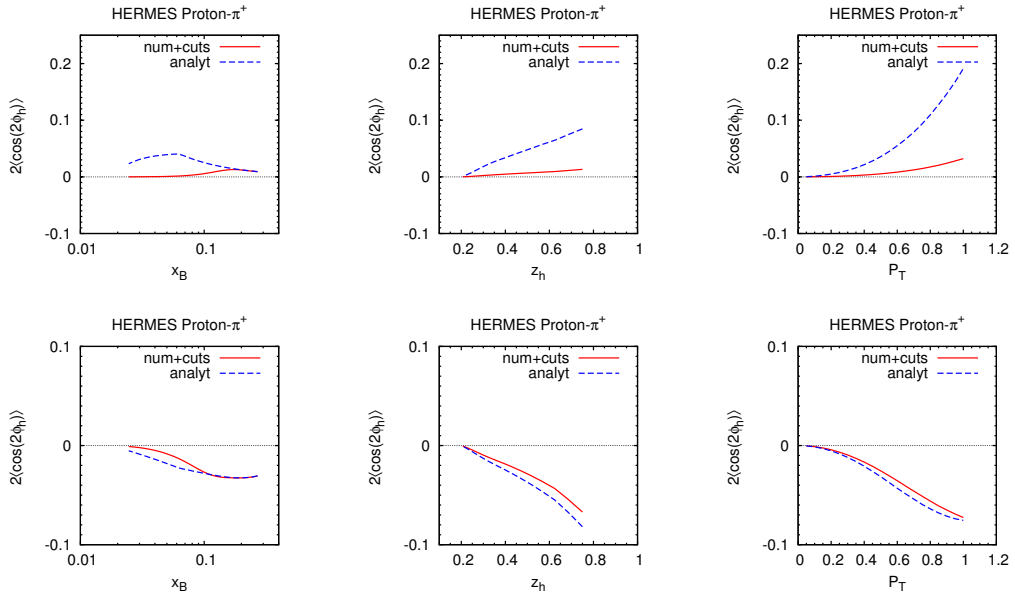

FIG. 12: In the upper panels we show the twist-4 Cahn contribution to the $\langle \cos 2\phi_h \rangle$ azimuthal modulation for π^+ production at HERMES as a function of x_B, z_h and P_T, in the lower panels the twist-2 Boer-Mulders contribution to the $\langle \cos 2\phi_h \rangle$ azimuthal modulation for π^+ production at HERMES, again as a function of x_B (left plot), z_h (central plot) and P_T (right plot).Ref. [34].

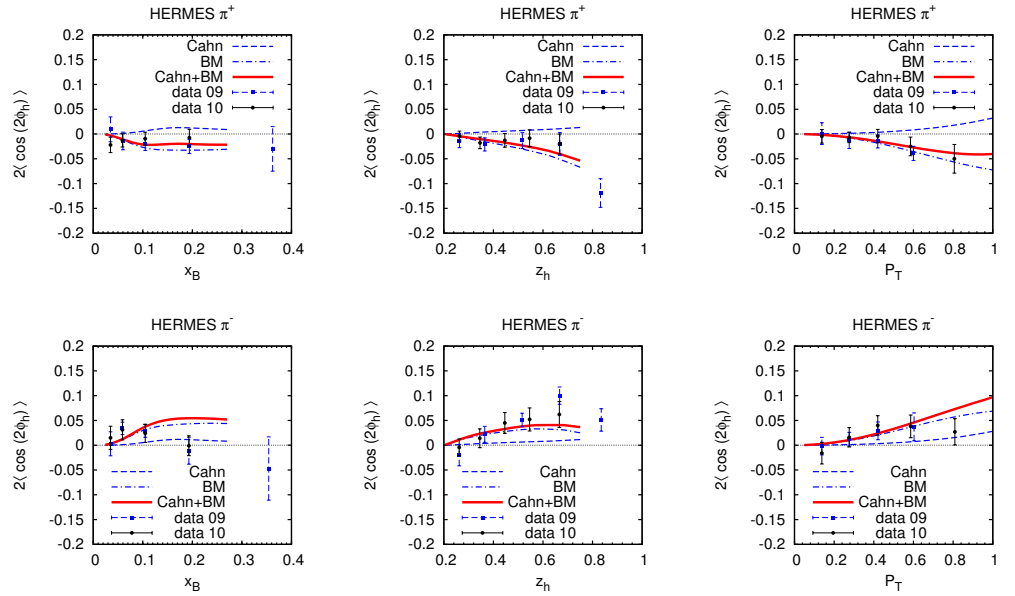

FIG. 13: Boer-Mulders and Cahn contributions to the $\langle \cos 2\phi_h \rangle$ azimuthal modulation for π^+ (upper panel) and π^- (lower panel) production at HERMES as a function of x_B (left plot), z_h (central plot) and P_T (right plot). Experimental data are from Refs. [23, 33, 34].

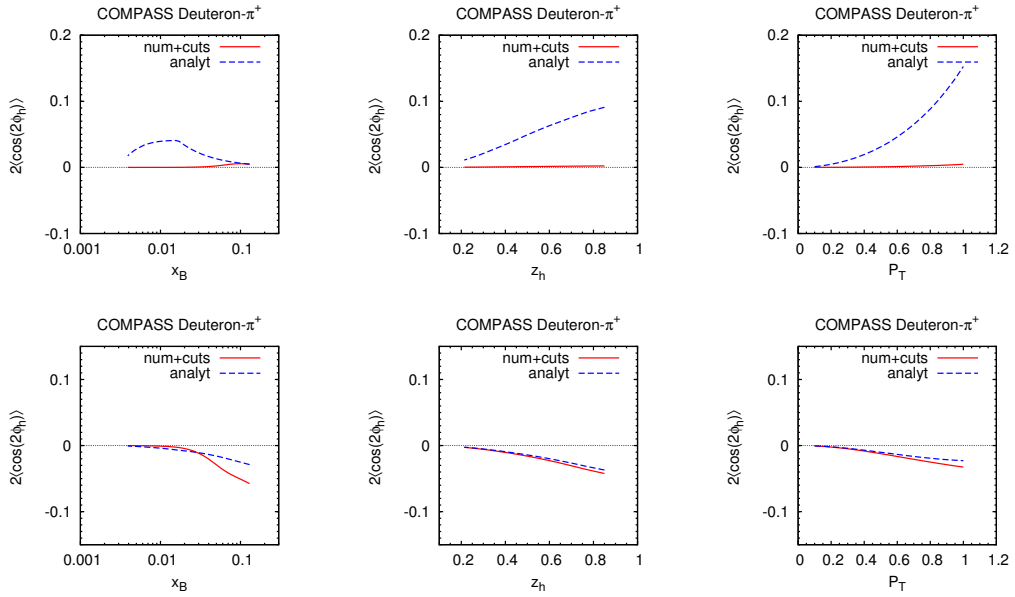

FIG. 14: In the upper panels we show the twist-4 Cahn contribution to the $\langle \cos 2\phi_h \rangle$ azimuthal modulation for π^+ production at COMPASS (deuteron target) as a function of x_B, z_h and P_T, in the lower panels the twist-2 Boer-Mulders contribution to the $\langle \cos 2\phi_h \rangle$ azimuthal modulation for π^+ production at HERMES again as a function of x_B (left plot), z_h (central plot) and P_T (right plot). data are from Ref. [37].

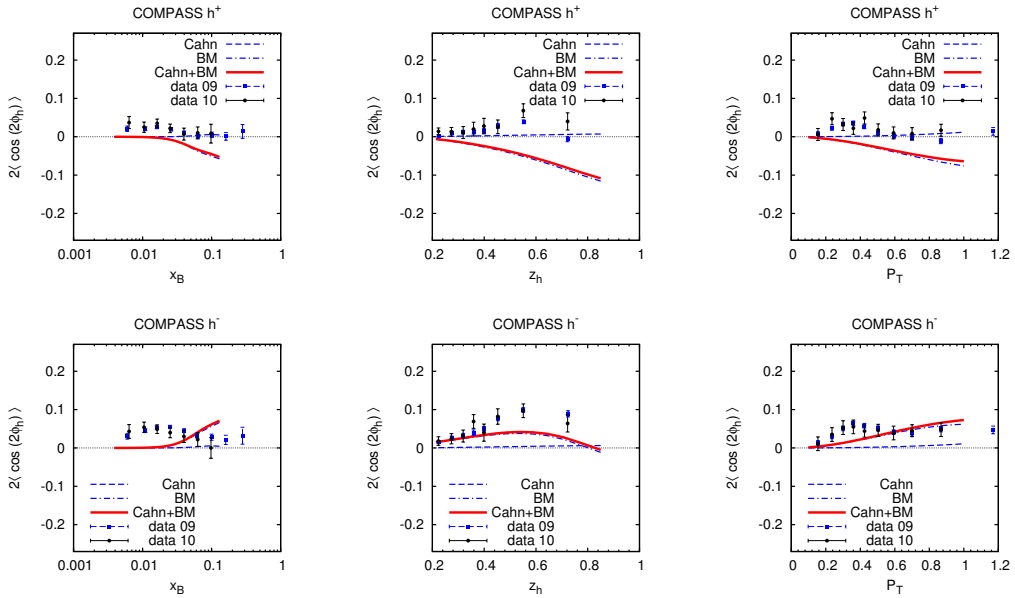

FIG. 15: Boer-Mulders and Cahn contributions to the $\langle \cos 2\phi_h \rangle$ azimuthal modulation for π^+ (upper panel) and π^- (upper panel) production at COMPASS (deuteron target) as a function of x_B (left plot), z_h (central plot) and P_T (right plot). Experimental data are from Ref. [35–37].

IV. CONCLUSIONS

In this paper we have studied SIDIS processes within a QCD parton model in the framework of TMD factorization; the dependence on the parton instrinsic transverse momentum is modelled through a Gaussian parametrization. By requiring the parton energy to be smaller than the energy of its parent hadron and preventing the parton to move backwards relatively to its parent hadron, we were able to determine an upper bound, $k_\perp^{max}(x_{_B}, Q^2)$, to the range of allowed values of $k_\perp$. Under these assumptions, we then re-calculated the three terms of the unpolarized SIDIS cross section (F_{UU}, $F_{UU}^{\cos\phi_h}$ and $F_{UU}^{\cos 2\phi_h}$), and the detected hadron average transverse momentum, $\langle P_T^2 \rangle$. Notice that we made sure that the unpolarized TMD distribution function, $f_{q/p}(x_{_B}, k_\perp)$, respected the proper normalization condition by requiring that the integral over $k_\perp$ in the restricted range $[0, k_\perp^{max}(x_{_B}, Q^2)]$ would still give the usual, collinear $f_{q/p}(x_{_B})$.

Although the effects of our $k_\perp$ - cuts over the azimuthal-independent term F_{UU} are almost irrelevant (only a slight difference in the F_{UU} dependence on P_T can be appreciated), we realized that the detected hadron average transverse momentum, $\langle P_T^2 \rangle$, and the azimuthal moments $\langle \cos\phi_h \rangle$ and $\langle \cos 2\phi_h \rangle$, are strongly sensitive to the constraints on the $k_\perp$ allowed values. In particular, by limiting the $k_\perp$ integration range, which effectively reduces the Gaussian width $\langle k_\perp^2 \rangle$ suppressing the asymmetry at low $x_{_B}$ (and consequently low Q^2) values, we improve the description of the $\langle \cos\phi_h \rangle$ azimuthal moment data from HERMES [23] and COMPASS [24] Collaborations, which were largely overestimated by the predictions obtained with an analytical $k_\perp$ integration over the unlimited $k_\perp$ range. Although the overall size of $\langle \cos\phi_h \rangle$, a factor 2 (ore more) smaller than that obtained without $k_\perp$ - cuts, is in good agreement with the most recent experimental data, some discrepancies remain in the shape of our predictions, which can be interpreted as a signal of the existence of higher twist contributions, that have been neglected in our study.

As far as the $\langle \cos 2\phi_h \rangle$ azimuthal moment is concerned, the situation remains slightly unresolved. Infact, while the effective reduction of the Gaussian width $\langle k_\perp^2 \rangle$ helps in obtaining a satisfactory agreement with HERMES measurements [34], some considerable inconsistencies remain in the description of the COMPASS data [37] which, instead, seem to suggest the presence of a much larger $k_\perp^2/Q^2$ Cahn contribution, that could only be achieved by increasing the average $k_\perp$. This might suggest the presence of nuclear smearing effects in the Li^6D target. COMPASS future data on a proton target will help to clarify this issue.

Finally, we observed a significant deviation of the detected hadron average transverse momentum, $\langle P_T^2 \rangle$, from the theoretical value $\langle P_T^2 \rangle_{_G} = \langle p_\perp^2 \rangle + z_h^2 \langle k_\perp^2 \rangle$, obtained by an analytical $k_\perp$ integration over the unlimited $k_\perp$ range. This is induced by two different mechanisms: on one side, the constraints we applied on the $k_\perp$ range of integration and, on the other side, the (inevitable) P_T cuts operated in the experimental analysis. In general, we predict a much flatter behaviour than that of $\langle P_T^2 \rangle_G$, but yet quite far from that suggested by the COMPASS analysis of Ref. [18]. This is indeed an issue to be further studied in future, as only very preliminary data are presently available from COMPASS, HERMES and JLab.

In this study, higher twist contributions were neglected, together with different mechanisms to generate the intrinsic transverse momenta, like soft gluon emission and TMD QCD evolution effects [38, 39]. Therefore more refined phenomenological descriptions are required to fix the details of such complex kinematics and dynamics. However, we have shown that some extra care should be taken when dealing with the present available experimental data, as they span a kinematical region in which $k_\perp/Q$ contributions can be large and are not safely under control, unless some limiting prescription over the allowed values of $k_\perp$ is applied.

Future experiments, like the Electron Ion Collider (EIC) [26, 27], where the experimental cuts and the Q^2 range would be easily adjustable in order to avoid unsafe kinematical regions, will definitely help us to gain a much clearer understanding of the three-dimensional structure of hadrons and, in particular, to disentangle higher order corrections from leading twist contributions.

V. ACKNOWLEDGEMENT

We would like to acknowledge useful discussions with Mauro Anselmino, Aram Kotzinian, Enzo Barone, Barbara Pasquini, and Leonard Gamberg. Authored by a Jefferson Science Associate, LLC under U.S. DOE Contract No. DE-AC05-06OR23177. The U.S. Government retains a non-exclusive, paid-up, irrevocable, world-wide license to publish or reproduce this manuscript for U.S. Government purposes.

Appendix A: Sudakov decomposition

For the treatment of the SIDIS kinematics, we use the usual Sudakov decomposition for four vectors:

$$v^\mu = v^+ n_+^\mu + v^- n_-^\mu + v_T^\mu \tag{A1}$$

where lightcone vectors n_+^μ and n_-^μ are

$$n_+^\mu = \frac{1}{\sqrt{2}}(1,0,0,1) \ , \quad n_-^\mu = \frac{1}{\sqrt{2}}(1,0,0,-1) \, , \tag{A2}$$

$$n_+ \cdot n_- = 1 \, , \qquad n_+^2 = n_-^2 = 0 \, . \tag{A3}$$

Using lightcone coordinates $a^\pm = 1/\sqrt{2}(a^0 \pm a^3)$, and notations $v^\mu = [v^-, v^+, \boldsymbol{v}_\perp]$ we can rewrite these vectors as

$$n_+^\mu = \left[0^-, 1^+, \mathbf{0}_\perp\right] \ , n_-^\mu = \left[1^-, 0^+, \mathbf{0}_\perp\right] \ , v_T^\mu = (0,0,\boldsymbol{v}_\perp). \tag{A4}$$

The product of two four vectors is then

$$v \cdot w = v^+ w^- + v^- w^+ - \boldsymbol{v}_\perp \cdot \boldsymbol{w}_\perp \tag{A5}$$

Note that $v_T^\mu \cdot v_{T\mu} = -v_\perp^2$ and $n_\pm \cdot v_T = 0$. The momentum four-vectors corresponding to the proton, the virtual photon and the struck quark are:

$$\begin{aligned} P^\mu &= P^- n_-^\mu + \frac{M^2}{2P^-} n_+^\mu \, , \\ q^\mu &= -\xi n_-^\mu + \frac{Q^2}{2\xi} n_+^\mu \, , \\ k^\mu &= xP^- n_-^\mu + \frac{k^2 + k_\perp^2}{2xP^-} n_+^\mu + k_T^\mu \, , \end{aligned} \tag{A6}$$

where the Sudakov vectors n_+, n_- are defined in Appendix A, $x = k^-/P^-$ is the quark light-cone momentum fraction and $\boldsymbol{k}_\perp$ is the quark intrinsic transverse momentum vector, see Fig. 1. Note that, according to the Trento conventions [28], P^- is the "large" component of the proton's momentum, i.e. along n_-^μ.

The variables of Eqs. (A6) then can be expressed as

$$\xi = \frac{Q^2}{\sqrt{2}W} \, , \qquad P^- = \frac{1}{\sqrt{2}}\left(W + \frac{Q^2}{W}\right) \, , \tag{A7}$$

and thus the proton and the virtual photon momenta can be written in the $\gamma^* - p$ c.m. frame, as functions of the invariants W and Q, in this way:

$$q^\mu = \left[-\frac{Q^2}{\sqrt{2}W}, \frac{W}{\sqrt{2}}, \mathbf{0}_\perp\right] = \left(P^0 - \frac{Q^2}{W}, \mathbf{0}_\perp, P^0\right) \, , \tag{A8}$$

$$P^\mu = \left[\frac{1}{\sqrt{2}}\left(W + \frac{Q^2}{W}\right), 0^+, \mathbf{0}_\perp\right] = \left(P^0, \mathbf{0}_\perp, -P^0\right) \, , \tag{A9}$$

where

$$P^0 = \frac{1}{2}\left(W + \frac{Q^2}{W}\right) \, . \tag{A10}$$

In the Generalised Parton Model the virtual photon scatters off an on-shell quark, thus we will neglect the virtuality of the quark k^2 and write the quark momentum in the $\gamma^* - p$ c.m. frame as:

$$k^\mu = \left[xP^-, \frac{k_\perp^2}{2xP^-}, \boldsymbol{k}_\perp\right] = \left(xP^0 + \frac{k_\perp^2}{4xP^0}, \boldsymbol{k}_\perp, -xP^0 + \frac{k_\perp^2}{4xP^0}\right) \, . \tag{A11}$$

Appendix B: Kinematical cuts

If not stated differently in the text, in our analysis we adopt the following kinematical cuts. For the HERMES experiment:

$$Q^2 \geq 1\ \mathrm{GeV}^2\,, \quad W^2 > 10\ \mathrm{GeV}^2\,, \quad 0.05 < P_T < 1.0\ \mathrm{GeV} \tag{B1}$$
$$0.023 < x_{_B} < 0.27\,, \quad 0.2 < z_h < 0.75\,, \quad 0.3 < y < 0.85\ , \tag{B2}$$

and for COMPASS:

$$Q^2 \geq 1\ \mathrm{GeV}^2\,, \quad W^2 > 25\ \mathrm{GeV}^2\,, \quad 0.1 < P_T < 1.0\ \mathrm{GeV} \tag{B3}$$
$$0.003 < x_{_B} < 0.13\,, \quad 0.2 < z_h < 0.85\,, \quad 0.2 \leq y \leq 0.9\ . \tag{B4}$$

Notice that hese kinematics correspond to the experimental cuts performed by these collaborations in their most recent analysis of the unpolarized azimuthal asymmetries [23, 37].

For the EMC kinematics we used the following kinematical cuts [22]:

$$Q^2 \geq 5\ \mathrm{GeV}^2\,, \quad W^2 < 90\ \mathrm{GeV}^2\,, \quad 0.01 < P_T < 2.0\ \mathrm{GeV} \tag{B5}$$
$$E_h > 5\mathrm{GeV}\,, \quad 0.1 < z_h < 0.9\,, \quad 0.2 \leq y \leq 0.8\ . \tag{B6}$$

The Electron Ion Collider (EIC) is a proposed facility [26, 27] to provide further information on the proton structures. Thus we used the following hypothetical kinematical configuration

$$Q^2 \geq 1 \ \text{ or } \ Q^2 \geq 10\ \mathrm{GeV}^2\,, \quad W^2 > 25\ \mathrm{GeV}^2\,, \quad 0.05 < P_T < 1\ \mathrm{GeV} \tag{B7}$$
$$0.2 < z_h < 0.8\,, \quad 0.05 \leq y \leq 0.8\,. \tag{B8}$$

[1] P. J. Mulders and R. D. Tangerman, Nucl. Phys. **B461**, 197 (1996).
[2] A. Bacchetta *et al.*, JHEP **02**, 093 (2007), hep-ph/0611265.
[3] M. Anselmino *et al.*, Phys. Rev. **D83**, 114019 (2011), arXiv:1101.1011.
[4] R. N. Cahn, Phys. Lett. **B78**, 269 (1978).
[5] R. N. Cahn, Phys. Rev. **D40**, 3107 (1989).
[6] X. Ji, J.-P. Ma, and F. Yuan, Phys. Rev. **D71**, 034005 (2005), hep-ph/0404183.
[7] M. Anselmino *et al.*, Phys. Rev. **D71**, 074006 (2005), hep-ph/0501196.
[8] M. Anselmino *et al.*, Phys. Rev. **D72**, 094007 (2005), hep-ph/0507181.
[9] M. Anselmino *et al.*, Phys. Rev. **D73**, 014020 (2006), hep-ph/0509035.
[10] M. Anselmino, M. Boglione, A. Prokudin, and C. Turk, Eur. Phys. J. **A31**, 373 (2007), hep-ph/0606286.
[11] M. Anselmino *et al.*, J. Phys. **G36**, 015007 (2009), arXiv:0710.1569.
[12] M. Anselmino *et al.*, Eur. Phys. J. **A39**, 89 (2009), arXiv:0805.2677.
[13] M. Anselmino *et al.*, Phys. Rev. **D75**, 054032 (2007), hep-ph/0701006.
[14] M. Anselmino *et al.*, Phys. Rev. **D79**, 054010 (2009), arXiv:0901.3078.
[15] P. Schweitzer, T. Teckentrup, and A. Metz, Phys. Rev. **D81**, 094019 (2010), arXiv:1003.2190.
[16] H. Avakian *et al.*, CLAS Collaboration, (2010), arXiv:1003.4549.
[17] M. Boglione and S. Melis, (2011), arXiv:1103.2084.
[18] J.-F. Rajotte, COMPASS Collaboration, (2010), arXiv:1008.5125.
[19] A. Airapetian *et al.*, HERMES Collaboration, Phys. Lett. **B684**, 114 (2010), arXiv:0906.2478.
[20] F. Giordano, (2008), DESY-THESIS-2008-030.
[21] M. Osipenko *et al.*, CLAS Collaboration, Phys. Rev. **D80**, 032004 (2009), arXiv:0809.1153.
[22] J. Ashman *et al.*, European Muon Collaboration, Z. Phys. **C52**, 361 (1991).
[23] F. Giordano and R. Lamb, HERMES Collaboration, PoS **DIS2010**, 106 (2010).
[24] G. Sbrizzai, COMPASS Collaboration, (2009), arXiv:0902.0578.
[25] V. Barone, S. Melis, and A. Prokudin, Phys. Rev. **D81**, 114026 (2010), arXiv:0912.5194.
[26] A. Deshpande, R. Milner, R. Venugopalan, and W. Vogelsang, Ann. Rev. Nucl. Part. Sci. **55**, 165 (2005), hep-ph/0506148.
[27] T. Horn, P. Nadel-Turonski, and C. Weiss, (2009), arXiv:0908.1999.
[28] A. Bacchetta, U. D'Alesio, M. Diehl, and C. A. Miller, Phys. Rev. **D70**, 117504 (2004), hep-ph/0410050.
[29] A. Bacchetta, M. Boglione, A. Henneman, and P. Mulders, Phys.Rev.Lett. **85**, 712 (2000), hep-ph/9912490.
[30] M. Gluck, E. Reya, and A. Vogt, Eur. Phys. J. **C5**, 461 (1998), hep-ph/9806404.

[31] D. de Florian, R. Sassot, and M. Stratmann, Phys. Rev. **D75**, 114010 (2007), hep-ph/0703242.
[32] M. Anselmino *et al.*, Nucl. Phys. Proc. Suppl. **191**, 98 (2009), arXiv:0812.4366.
[33] R. Lamb and F. Giordano, HERMES Collaboration, Nucl. Phys. **A827**, 225c (2009).
[34] F. Giordano and R. Lamb, HERMES Collaboration, AIP Conf. Proc. **1149**, 423 (2009), arXiv:0901.2438.
[35] W. Kafer, COMPASS, (2008), arXiv:0808.0114.
[36] A. Bressan, COMPASS, (2009), arXiv:0907.5511.
[37] G. Sbrizzai, COMPASS Collaboration, (2010), arXiv:1012.4910.
[38] S. M. Aybat and T. C. Rogers, (2011), arXiv:1101.5057.
[39] J. Collins, "Foundations of Perturbative QCD" , Cambridge University Press, Cambridge (2011).